# QuickSampling v1.0: a robust and simplified pixel-based multiple-point simulation approach

Mathieu Gravey[1], Grégoire Mariethoz[1]

[1] University of Lausanne, Faculty of Geosciences and Environment, Institute of Earth Surface Dynamics, Switzerland

*Correspondence to*: Mathieu Gravey (mathieu.gravey@unil.ch)

## Highlights

- A new approach is proposed for pixel-based multiple-point geostatistics simulation.
- The method is flexible and straightforward to parametrize.
- It natively handles continuous and multivariate simulations.
- High computational performance with predictable simulation times.
- A free and open-source implementation is provided.

## Abstract

Multiple-point geostatistics enable the realistic simulation of complex spatial structures by inferring statistics from a training image. These methods are typically computationally expensive and require complex algorithmic parametrizations. The approach that is presented in this paper is easier to use than existing algorithms, as it requires few independent algorithmic parameters. It is natively designed for handling continuous variables, and quickly implemented by capitalizing on standard libraries. The algorithm can handle incomplete training images of any dimensionality, with categorical or/and continuous variables, and stationarity is not explicitly required. It is possible to perform unconditional or conditional simulations, even with exhaustively informed covariates. The method provides new degrees of freedom by allowing kernel weighting for pattern matching. Computationally, it is adapted to modern architectures and runs in constant time. The approach is benchmarked against a state-of-the-art method. An efficient open-source implementation of the algorithm is released and can be found here (https://github.com/GAIA-UNIL/G2S), to promote reuse and further evolution.

## Keywords

Multiple-point statistics, stochastic simulation, continuous variable, training image, cross-correlation, Fourier transform.

## 1. Introduction

Geostatistics is used widely to generate stochastic random fields for modeling and characterizing spatial phenomena such as Earth surface features and geological structures. Commonly used methods, such as the sequential Gaussian simulation (Gómez-Hernández and Journel, 1993) and turning bands algorithms (Matheron, 1973), are based on kriging ( e.g., Graeler et al., 2016; Li and Heap, 2014; Tadić et al., 2017; 2015). This family of approaches implies spatial relations using exclusively pairs of points and expresses these relations using

covariance functions. In the last two decades, multiple point statistics (MPS) emerged as a method for representing more complex structures using high-order nonparametric statistics (Guardiano and Srivastava, 1993). To do so, MPS algorithms rely on training images, which are images with similar characteristics to the modeled area. Over the last decade, MPS has been used for stochastic simulation of random fields in a variety of domains such as geological modeling (e.g., Barfod et al., 2018; Strebelle et al., 2002), remote sensing data processing (e.g., Gravey et al., 2019; Yin et al., 2017), stochastic weather generation (e.g., Oriani et al., 2017; Wojcik et al., 2009), geomorphological classification (e.g., Vannametee et al., 2014) and climate model downscaling (a domain that has typically been the realm of kriging-based methods ( e.g., Bancheri et al., 2018; Jha et al., 2015; Latombe et al., 2018)).

In the world of MPS simulations, one can distinguish two types of approaches. The first category is the patch-based methods, where complete patches of the training image are imported into the simulation. This category includes methods such as SIMPAT (Arpat and Caers, 2007) and DISPAT (Honarkhah and Caers, 2010), which are based on building databases of patterns, and image quilting (Mahmud et al., 2014), which uses an overlap area to identify patch candidates, which are subsequently assembled using an optimal cut. CCSIM (Tahmasebi et al., 2012) uses cross-correlation to rapidly identify optimal candidates. More recently, Li (2016) proposed a solution that uses graph-cuts to find an optimal cut between patches, which has the advantage of operating easily and efficiently independently of the dimensionality of the problem. Tahmasebi (2017) propose as a solution that is based on “warping” in which the new patch is distorted to match the previously simulated areas. For a multivariate simulation with an informed variable, Hoffimann (2017) presented an approach for selecting a good candidate based on the mismatch of the primary variable, and on the mismatch rank of the candidate patches for auxiliary variables. Although patch-based approaches are recognized to be fast, they are typically difficult to use in the presence of dense conditioning data. Furthermore, patch-based approaches often suffer from a lack of variability due to the pasting of large areas of the training image, which is a phenomenon that is called verbatim copy. Verbatim copy (Mariethoz and Caers, 2014) refers to the phenomenon whereby the neighbor of a pixel in the simulation is the neighbor in the training image. This results in large parts of the simulation that are identical to the training image.

The second category of MPS simulation algorithms consists of pixel-based algorithms, which import a single pixel at the time instead of full patches. These methods are typically slower than patch-based methods. However, they do not require a procedure for the fusion of patches, such as an optimal cut, and they allow more flexibility in handling conditioning data. Furthermore, in contrast to patch-based methods, pixel-based approaches rarely produce artifacts when dealing with complex structures. The first pixel-based MPS simulation algorithm was ENESIM, which was proposed by Guardiano and Srivastava, 1993, where for a given categorical neighborhood – usually small – all possible matches in the training image are searched. The conditional distribution of the pixel to be simulated is estimated based on all matches, from which a value is sampled. This approach could originally handle only a few neighbors and a relatively small training image; otherwise, the computational cost would become prohibitive and the number of samples insufficient for estimating the conditional distribution. Inspired by research in computer graphics, where similar techniques are developed

for texture synthesis (Mariethoz and Lefebvre, 2014), an important advance was the development of SNESIM (Strebelle, 2002), which proposes storing in advance all possible conditional distributions in a tree structure and using a multigrid simulation path to handle large structures. With IMPALA, Straubhaar (2011) proposed reducing the memory cost by storing information in lists rather than in trees. Another approach is direct sampling (DS) (Mariethoz et al., 2010), where the estimation and the sampling of the conditional probability distribution are bypassed by sampling directly in the training image, which incurs a very low memory cost. DS enabled the first use of pixel-based simulations with continuous variables. DS can use any distance formulation between two patterns; hence, it is well suited for handling various types of variables and multivariate simulations.

In addition to its advantages, DS has several shortcomings: DS requires a threshold – which is specified by the user – that enables the algorithm to differentiate good candidate pixels in the training image from bad ones based on a predefined distance function. This threshold can be highly sensitive and difficult to determine and often dramatically affects the computation time. This results in unpredictable computation times, as demonstrated by Meerschman (2013). DS is based on the strategy of randomly searching the training image until a good candidate is identified (Shannon, 1948). This strategy is an advantage of DS; however, it can also be seen as a weakness in the context of modern computer architectures. Indeed, random memory access and high conditionality can cause 1) suboptimal use of the instruction pipeline, 2) poor memory prefetch, 3) substantial reduction of the useful memory bandwidth and 4) impossibility of using vectorization ( Paul Shen, 2018). While the first two problems can be addressed with modern compilers and pseudorandom sequences, the last two are inherent to the current memory and CPU construction.

This paper presents a new and flexible pixel-based simulation approach, namely, QuickSampling (QS), which makes efficient use of modern hardware. Our method takes advantage of the possibility of decomposing the standard distance metrics that are used in MPS ($L^0, L^2$) as sums of cross-correlations. As a result, we can use fast Fourier transforms (FFTs) to quickly compute mismatch maps. To rapidly select candidate patterns in the mismatch maps, we use an optimized partial sorting algorithm. A free, open-source and flexible implementation of QS is available, which is interfaced with most common programming languages (C/C++, MATLAB, R, and Python 3).

The remainder of this paper is structured as follows: Section 2 presents the proposed algorithm with an introduction to the general method of sequential simulation, the mismatch measurement using FFTs and the sampling approach of using partial sorting followed by methodological and implementation optimizations. Section 3 evaluates the approach in terms of quantitative and qualitative metrics via simulations and conducts benchmark tests against DS, which is the only other available approach that can handle continuous pixel-based simulations. Section 4 discusses the strengths and weaknesses of QS and provides guidelines. Finally, guidelines and the conclusions of this work are presented in Section 5.

# 2. Methodology and Implementation

## 2.1.Pixel-based sequential simulation

We recall the main structure of pixel-based MPS simulation algorithms (Mariethoz and Caers, 2014, p.156), which is summarized and adapted for QS in Pseudocode 1. The key difference between existing approaches is in lines 3 and 4 of Pseudocode 1, when candidate patterns are selected. This task is the most time-consuming in many MPS algorithms and we focus only on computing it in a way that reduces its cost and minimizes the parameterization.

Pseudocode 1: QS Algorithm

Inputs:

$T$ the training images

$S$ the simulation grid, including the conditioning data

$P$ the simulation path

The choice of pattern metric

1. **For** each unsimulated pixel $x$ following the path $P$:
2. Find the neighborhood $N(x)$ in $S$ that contains all previously simulated or conditioning nodes in a specified radius
3. Compute the mismatch map between $T$ and $N(x)$: Section 2.3
4. Select a good candidate using quantile sorting over the mismatch map: Section 2.4
5. Assign the value of the selected candidate to $x$ in $S$
6. **End**

## 2.2. Decomposition of common mismatch metrics as sums of products

Distance-based MPS approaches are based on pattern matching (Mariethoz and Lefebvre, 2014). Here, we rely on the observation that many common matching metrics can be expressed as weighted sums of the pixelwise mismatch $\varepsilon$. This section explores the pixelwise errors for a single variable and for multiple variables. For a single variable, the mismatch metric $\varepsilon$ between two pixels is the distance between two scalars or two classes. In the case of many variables, it is a distance between two vectors that are composed by scalars, by classes, or by a combination of the two. Here, we focus on distance metrics that can be expressed in the following form:

*Equation 1*

$$\varepsilon(a,b) \propto \sum_{j\in\mathcal{J}} f_j(a).\, g_j(b)$$

where $a$ and $b$ represent the values of two univariate pixels and $f_j$ and $g_j$ are functions that depend on the chosen metric. $\mathcal{J}$ is defined by the user depending on the metric used. Here, we use the proportion symbol because we are interested in relative metrics rather than absolute metrics, namely, the objective is to rank the candidate patterns. We show below that many of the common metrics or distances that are used in MPS can be expressed as Equation 1.

For the simulation of continuous variables, the most commonly used mismatch metric is the $L^2$-norm, which can be expressed as follows:

*Equation 2*

$$\varepsilon_{L^2}(a,b) = (a-b)^2 = a^2 - 2ab + b^2$$

Using Equation 1, this $L^2$-norm can be decomposed into the following series of functions $f_j$ and $g_j$:

$f_0 : x \to x^2$ $\quad$ $g_0 : x \to 1$

$f_1 : x \to -2x$ $\quad$ $g_1 : x \to x$

$f_2 : x \to 1$ $\quad$ $g_2 : x \to x^2$

A similar decomposition is possible for the $L^0$ -norm (also called Hamming distance), which is commonly used for the simulation of categorical variables. The Hamming distance measures the dissimilarity between two lists by counting the number of elements that have different categories (Hamming, 1950). Example the dissimilarity between a,b,b,c,b,a and a,c,b,a,c,a is 0,1,0,1,1,0 and the associated Hamming distance is 3.

*Equation 3*

$$\varepsilon_{L^0}(a,b) = (a-b)^0 = 1 - \sum_{j\in\mathcal{C}} \left(\delta_{a,j}.\delta_{b,j}\right) \propto \sum_{j\in\mathcal{C}} \delta_{a,j}.\delta_{b,j}$$

where $\delta_{x,y}$ is the Kronecker delta between $x$ and $y$, which is 1 if $x$ equals $y$ and 0 otherwise, and $\mathcal{C}$ is the set of all possible categories of a specified variable. Here $\mathcal{J} = \mathcal{C}$.

Using Equation 1, this $L^0$ distance can be decomposed (Arpat and Caers, 2007) into the following series of functions $f_j$ and $g_j$ :

$f_j : x \to -\delta_{xj}$

$g_j : x \to \delta_{xj}$

with a new pair of $f_j$ and $g_j$ for each class $j$ of $\mathcal{C}$.

For multivariate pixels, such as a combination of categorical and continuous values, the mismatch $\varepsilon$ can be expressed as a sum of univariate pixelwise mismatches.

*Equation 4*

$$\varepsilon(\boldsymbol{a},\boldsymbol{b}) \propto \sum_{i\in\mathcal{I}} \sum_{j\in\mathcal{J}_i} f_j(a_i).g_j(b_i)$$

where $\boldsymbol{a}$ and $\boldsymbol{b}$ are the compared vectors and $a_i$ and $b_i$ are the individual components of $\boldsymbol{a}$ and $\boldsymbol{b}$. $\mathcal{J}_i$ represents the set related to the metric used for the $i^{st}$ variable, and $\mathcal{I}$ represents the set of variables.

## 2.3. Computation of a mismatch map for an entire pattern

The approach that is proposed in this work is based on computing a mismatch map in the TI for each simulated pixel. The mismatch map is a grid that represents the pattern-wise mismatch for each location of the training image and enables the fast identification of a good candidate, as shown by the red circle in Figure 1.

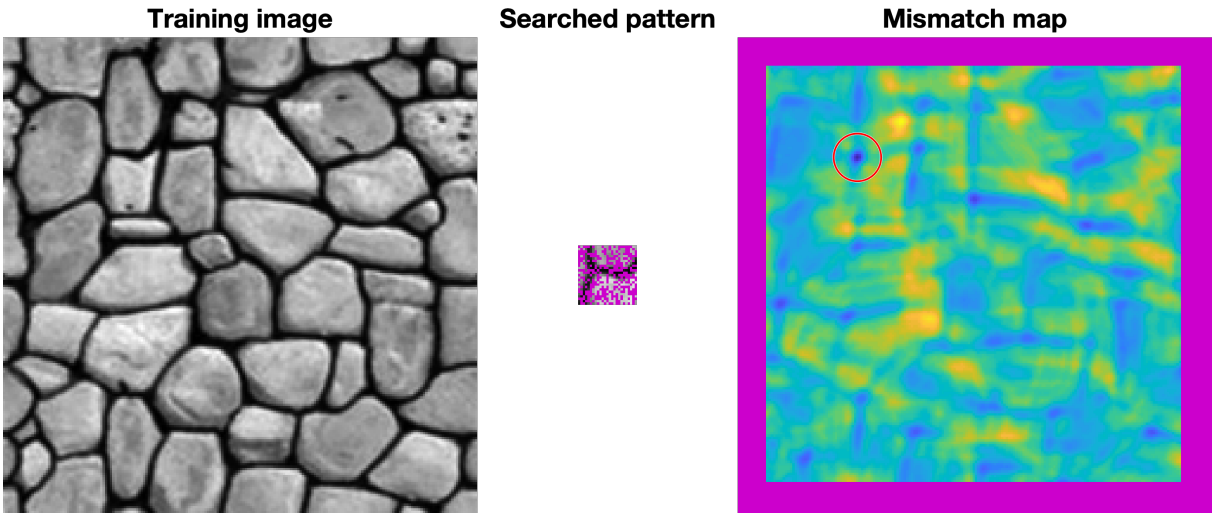


*Figure 1 Example of a mismatch map for an incomplete pattern. Blue represents good matches, yellow bad matches and purple missing and unusable (border effect) data. The red circle highlights the minimum of the mismatch map, which corresponds to the location of the best candidate.*

If we consider the neighborhood $N(s)$ around the simulated position $s$, then we can express a weighted dissimilarity between $N(s)$ and a location in the TI $N(t)$:

*Equation 5*

$$\mathrm{E}\big(N(t), N(s)\big) = \sum_{\boldsymbol{l} \in N(t,s)} \omega_{\boldsymbol{l}} \varepsilon\big(N_{\boldsymbol{l}}(t), N_{\boldsymbol{l}}(s)\big)$$

where $N(t,s) = \{l \,|N_{\boldsymbol{l}}(t)\ and\ N_{\boldsymbol{l}}(s)\ exist\}$

and $N_{\boldsymbol{l}}(p)$ is the neighbors of $p$ ($p$ can represent either $s$ or $t$) with a relative displacement $l$ from $p$, therefore $N(p) = \{l \mid N_{\boldsymbol{l}}(p)\}$, $\boldsymbol{l}$ is the lag vector that defines the relative position of each value within $N$, and $\omega_{\boldsymbol{l}}$ is a weight for each pixelwise error according to the lag vector $\boldsymbol{l}$. By extension, $\omega$ is the matrix of all weights, which we call the weighting kernel or, simply, the kernel. E represents the mismatch between patterns that are centered on $s$ and $t \in T$, where $T$ is the training image.

Some lags may not correspond to a value, for example, due to edge effects in the considered images or because the patterns are incomplete. Missing patterns are inevitable during the course of a simulation using a sequential path. Furthermore, in many instances, there can be missing areas in the training image. This is addressed by creating an indicator variable to be used as a mask, which equals 1 at informed pixels and 0 everywhere else:

*Equation 6*

$$\mathbb{1}_{\boldsymbol{l}}(p) = \begin{cases} 1\ if\ N_{\boldsymbol{l}}(p)\ is\ informed \\ 0\ otherwise \end{cases}$$

Let us first consider the case in which for a specified position, either all or no variables are informed. Expressing the presence of data as a mask enables the gaps to be ignored because the corresponding errors are multiplied by zero.

Then, Equation 5 can be expressed as follows:

*Equation 7*

$$\mathrm{E}\big(N(t), N(s)\big) = \sum_{\boldsymbol{l}} \omega_{\boldsymbol{l}}.\, \mathbb{1}_{\boldsymbol{l}}(t).\, \mathbb{1}_{\boldsymbol{l}}(s).\, \varepsilon\big(N_{\boldsymbol{l}}(t), N_{\boldsymbol{l}}(s)\big)$$

. Combining Equation 4 and Equation 7, we get:

*Equation 8*

$$\begin{aligned}
\mathrm{E}\big(N(t), N(s)\big) &\propto \sum_{\boldsymbol{l}} \omega_{\boldsymbol{l}}.\, \mathbb{1}_{\boldsymbol{l}}(t).\, \mathbb{1}_{\boldsymbol{l}}(s) \sum_{i\in\mathcal{I}} \sum_{j\in\mathcal{J}_i} f_j(N_{\boldsymbol{l}}(t)_i).\, g_j(N_{\boldsymbol{l}}(s)_i) \\
&= \sum_{\boldsymbol{l}} \sum_{i\in\mathcal{I}} \sum_{j\in\mathcal{J}_i} \omega_{\boldsymbol{l}}.\, \mathbb{1}_{\boldsymbol{l}}(t).\, \mathbb{1}_{\boldsymbol{l}}(s).\, f_j(N_{\boldsymbol{l}}(t)_i).\, g_j(N_{\boldsymbol{l}}(s)_i) \\
&= \sum_{i\in\mathcal{I}} \sum_{j\in\mathcal{J}_i} \sum_{\boldsymbol{l}} \omega_{\boldsymbol{l}}.\, \Big(\mathbb{1}_{\boldsymbol{l}}(t).\, f_j(N_{\boldsymbol{l}}(t)_i)\Big).\, \Big(\mathbb{1}_{\boldsymbol{l}}(s).\, g_j(N_{\boldsymbol{l}}(s)_i)\Big) \\
&= \sum_{i\in\mathcal{I}} \sum_{j\in\mathcal{J}_i} \sum_{\boldsymbol{l}} \Big(\mathbb{1}_{\boldsymbol{l}}(t).\, f_j(N_{\boldsymbol{l}}(t)_i)\Big).\, \Big(\omega_{\boldsymbol{l}}.\, \mathbb{1}_{\boldsymbol{l}}(s).\, g_j(N_{\boldsymbol{l}}(s)_i)\Big)
\end{aligned}$$

.

After rewriting, Equation 8 can be expressed as a sum of cross-correlations that encapsulate spatial dependencies, using the cross-correlation definition $f \star g = \sum_l f_l.\, g_l$, as follows:

*Equation 9*

$$\mathrm{E}\big(N(t), N(s)\big) \propto \sum_{i\in\mathcal{I}} \sum_{j\in\mathcal{J}_i} \Big(\mathbb{1}(t) \circ f_j(N(t)_i)\Big) \star \Big(\omega \circ \mathbb{1}(s) \circ g_j(N(s)_i)\Big)$$

where $\omega$ and $\mathbb{1}(.)$ represent the matrices that are formed by $\omega_{\boldsymbol{l}}$ and $\mathbb{1}_{\boldsymbol{l}}(.)$ for all possible vectors $\boldsymbol{l}$, $\star$ denotes the cross-correlation operator, and $\circ$ is the element-wise product (or Hadamard-product).

Finally, with $T = \{T_i, i \in \mathcal{I}\}$, $T_i$ represents the training image for the i-th variable, and by applying cross-correlations for all positions $t \in T$, we obtain a mismatch map, which is expressed as:

*Equation 10*

$$\mathrm{E}\big(T, N(s)\big) \propto \sum_{i\in\mathcal{I}} \sum_{j\in\mathcal{J}_i} \Big(\mathbb{1}(T) \circ f_j(T_i)\Big) \star \Big(\omega \circ \mathbb{1}(s) \circ g_j(N(s)_i)\Big)$$

. The term $\mathbb{1}(T)$ allows the consideration of the possibility of missing data in the training image $T$.

Let us consider the general case in which only some variables are informed and the weighting can vary for each variable. Equation 10 can be extended for this case by defining separate masks and weights $\omega_i$ for each variable:

*Equation 11*

$$\mathrm{E}\big(T, N(s)\big) \propto \sum_{i \in \mathcal{I}} \sum_{j \in \mathcal{J}_i} \Big(\mathbb{1}(T_i) \circ f_j(T_i)\Big) \star \Big(\omega_i \circ \mathbb{1}(s_i) \circ g_j(N(s)_i)\Big)$$

. Equation 11 can be expressed using the convolution theorem applied to cross-correlation:

*Equation 12*

$$\mathrm{E}\big(T, N(s)\big) \propto \sum_{i \in \mathcal{I}} \sum_{j \in \mathcal{J}_i} \mathcal{F}^{-1}\left\{\overline{\mathcal{F}\{\mathbb{1}(T_i) \circ f_j(T_i)\}} \circ \mathcal{F}\{\omega_i \circ \mathbb{1}(s_i) \circ g_j(N(s)_i)\}\right\}$$

, where $\mathcal{F}$ represents the Fourier transform, $\mathcal{F}^{-1}$ the inverse transform, and $\bar{x}$ the conjugate of $x$.

By linearity of the Fourier transform, the summation can be performed in Fourier space, thereby reducing the number of transformations:

*Equation 13*

$$\mathrm{E}\big(T, N(s)\big) \propto \mathcal{F}^{-1}\left\{\sum_{i \in \mathcal{I}} \sum_{j \in \mathcal{J}_i} \overline{\mathcal{F}\{\mathbb{1}(T_i) \circ f_j(T_i)\}} \circ \mathcal{F}\{\omega_i \circ \mathbb{1}(s_i) \circ g_j(N(s)_i)\}\right\}$$

. Equation 13 is appropriate for modern computers, which are well-suited for computing FFTs (Cooley et al., 1965; Gauss, 1799). Currently, FFTs are well implemented in highly optimized libraries (Rodríguez, 2002). Equation 13 is the expression that is used in our QS implementation because it reduces the number of Fourier transforms, which are the most computationally expensive operations of the algorithm. One issue with the use of FFTs is that the image $T$ is typically assumed to be periodic. However, in most practical applications, it is not periodic. This can be simply addressed by cropping the edges of $E\big(T, N(s)\big)$ or by adding a padding around $T$.

The computation of the mismatch map (Equation 13) is deterministic; as a result, it incurs a constant computational cost that is independent of the pixel values. Additionally, Equation 13 is expressed without any constraints on the dimensionality. Therefore, it is possible to use the *n*-dimensional FFTs that are provided in the above libraries to perform *n*-dimensional simulations without changing the implementation.

## 2.4. Selection of candidates based on a quantile

The second contribution of this work is the *k*-sampling strategy for selecting a simulated value among candidates. The main idea is to use the previously calculated mismatch map to select a set of potential candidates that are defined by the $k$ smallest (i.e. a quantile) values of E. Once this set has been selected, we randomly draw a sample from this pool of candidates. This differs

from strategies that rely on a fixed threshold, which can be cumbersome to determine. This strategy is highly similar to the ε-replicate strategy that is used in image quilting (Mahmud et al., 2014) in that we reuse and extend to satisfy the specific requirements of QS. It has the main advantage of rescaling the acceptance criterion according to the difficulty; i.e. the algorithm is more tolerant of rare patterns while requiring very close matches for common patterns.

In detail, the candidate selection procedure is as follows: All possible candidates are ranked according to their mismatch and one candidate is randomly sampled among the $k$ best. This number $k$ can be seen as a quantile over the training dataset. However, parameter $k$ has the advantage of being an easy representation for users, who can associate $k = 1$ with the best candidate, $k = 2$ with the two best candidates, etc. For fine-tuning parameter $k$, the sampling strategy can be extended to non-integer values of $k$ by sampling the candidates with probabilities that are not uniform. For example, if the user sets $k = 1.5$, the best candidate has a probability of 2/3 of being sampled and the second best a probability of 1/3. For $k = 3.2$, (Figure 2) each of the 3 best candidates are sampled with an equal probability of 0.3125 and the 4th best with a probability of 0.0625. This feature is especially useful for tuning $k$ between 1 and 2 and for avoiding a value of $k = 1$, which can result in the phenomenon of verbatim copy.

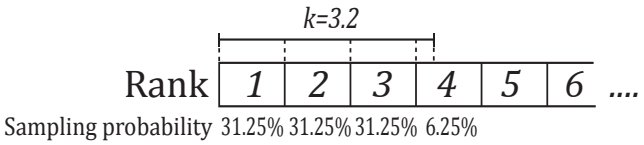


*Figure 2 Illustration of the k-sampling strategy*

An alternative sampling strategy for reducing the simulation time is presented in Appendix A.3. However, this strategy can result in a reduction in the simulation quality.

The value of non-integer k-values is not only in the fine tuning of parameters. It also allows direct comparisons between QS and DS. Indeed, under the hypothesis of a stationary training image, using DS with a given max fraction of scanned training image ($f$) and a threshold ($t$) of 0 is statistically similar to using QS with k=$1/f$. In both situations, the best candidate is sampled in a fraction $f$ of the training image.

## 2.5. Simplifications in the case of a fully informed training image

In many applications, spatially exhaustive TIs are available. In such cases, the equations above can be simplified by dropping constant terms from Equation 1, thereby resulting in a simplified form for Equation 13. Here, we take advantage of the ranking to know that a constant term will not affect the result.

As in Tahmasebi (2012), in the $L^2$-norm, we drop the squared value of the searched pattern, namely, $b^2$, from Equation 2. Hence, we can express Equation 4 as follows:

*Equation 14*

$$\varepsilon(\boldsymbol{a},\boldsymbol{b}) = \sum_{i\in\mathcal{I}} a_i^2 - 2\sum_{i\in\mathcal{I}} a_i.\, b_i$$

The term $a^2$, which represents the squared value of the candidate pattern in the TI, differs among training image locations and, therefore, cannot be removed. Indeed, the assumption that $\sum a^2$ is constant is only valid under a strict stationarity hypothesis on the scale of the search pattern. While this hypothesis might be satisfied in some cases (as in Tahmasebi et al., 2012), we do not believe it is generally valid. Via the same approach, Equation 3 can be simplified by removing the constant terms; then, we obtain the following for the $L^0$-norm:

*Equation 15*

$$\varepsilon(\boldsymbol{a},\boldsymbol{b}) = -\sum_{i\in\mathcal{I}}\sum_{j\in\mathcal{C}} \delta_{a_i,j}.\,\delta_{b_i,j}$$

.

## 2.6. Efficient Implementation

An efficient implementation of QS was achieved by 1) performing precomputations, 2) implementing an optimal partial sorting algorithm for selecting candidates and 3) optimal coding and compilation. These are described below.

According to Equation 13, $\overline{\mathcal{F}\{\mathbb{1}(T_i)\circ f_j(T_i)\}}$ is independent of the searched pattern $N(s)$. Therefore, it is possible to precompute it at the initialization stage for all $i$ and $j$. This improvement typically reduces the computation time for an MPS simulation by a factor of at least 2.

In the QS algorithm, a substantial part of the computation cost is incurred in identifying the $k$ best candidates in the mismatch map. In the case of non-integer $k$, the upper limit $\lceil k \rceil$ is used. Identifying the best candidates requires sorting the values of the mismatch map and retaining the candidates in the top $k$ ranks. For this, an efficient sorting algorithm is needed. The operation of finding the $k$ best candidates can be implemented with a partial sort, in which only the elements of interest are sorted, while the other elements remain unordered. This results in two sets: $\mathfrak{S}_s$ with the $k$ smallest elements and $\mathfrak{S}_l$ with the largest elements. The partial sort guarantees that $x \leq y \mid (x,y) \in \mathfrak{S}_s \times \mathfrak{S}_l$. More information about our implementation of this algorithm is available in Appendix A.1. Here, we use a modified vectorized online heap-based partial sort (Appendix A.1). With a complexity of $O(n.\ln(k))$, it is especially suitable for small values of $k$. Using the cache effect, the current implementation yields results that are close to the search of the best value (the smallest value of the array). The main limitation of standard partial sort implementations is that in the case of equal values, either the first or the last element is sampled. Here, we develop an implementation that can uniformly sample a position among similar values with a single scan of the array. This is important because systematically selecting the same position for the same pattern will reduce the conditional probability density function to a unique sample, thereby biasing the simulation.

Due to the intensive memory access by repeatedly scanning large training images, interpreted programming languages, such as MATLAB and Python, are inefficient for a QS implementation and, in particular, for a parallelized implementation. We provide a NUMA-aware (Blagodurov et al., 2010) and flexible C/C++/OpenMP implementation of QS that is highly optimized. Following the denomination of Mariethoz (2010), we use a path-level parallelization with a waiting strategy, which offers a good trade-off between performance and memory requirements. In addition, two node-level parallelization strategies are available: if many training images are used, a first parallelization is performed over the exploration of the training images; then, each FFT of the algorithm is parallelized using natively parallel FFT libraries.

The FFTw library (Frigo and Johnson, 2018) provides a flexible and performant architecture-independent framework for computing *n*-dimensional Fourier transformations. However, an additional speed gain of approximately 20% was measured by using the Intel MKL library (Intel Corporation, 2019) on compatible architectures. We also have a GPU implementation that uses clFFT for compatibility. Many Fourier transforms are sparse and, therefore, can easily be accelerated in *n*-dimensional cases with "partial FFT" since Fourier transforms of only zeros result in zeros.

# 3. Results

## 3.1. Simulation examples

This section presents illustrative examples for continuous and categorical case studies in 2D and in 3D. Additional tests are reported in Appendix 0. The parameters that are used for the simulations of Figure 3 are reported in Table 1.

The results show that simulation results are consistent with what is typically observed with state-of-the-art MPS algorithms. While simulations can accurately reproduce TI properties for relatively standard examples with repetitive structures (e.g., MV, Strebelle, and Folds), training images with long-range features (typically larger than the size of the TI) are more difficult to reproduce, such as in the Berea example. For multivariate simulations, the reproduction of the joint distribution is satisfactory, as observed in the scatterplots (Figure 3). More examples are available in Annex A4, in particular the Figure A2 for 2D examples and the Figure A3 for 3D examples.

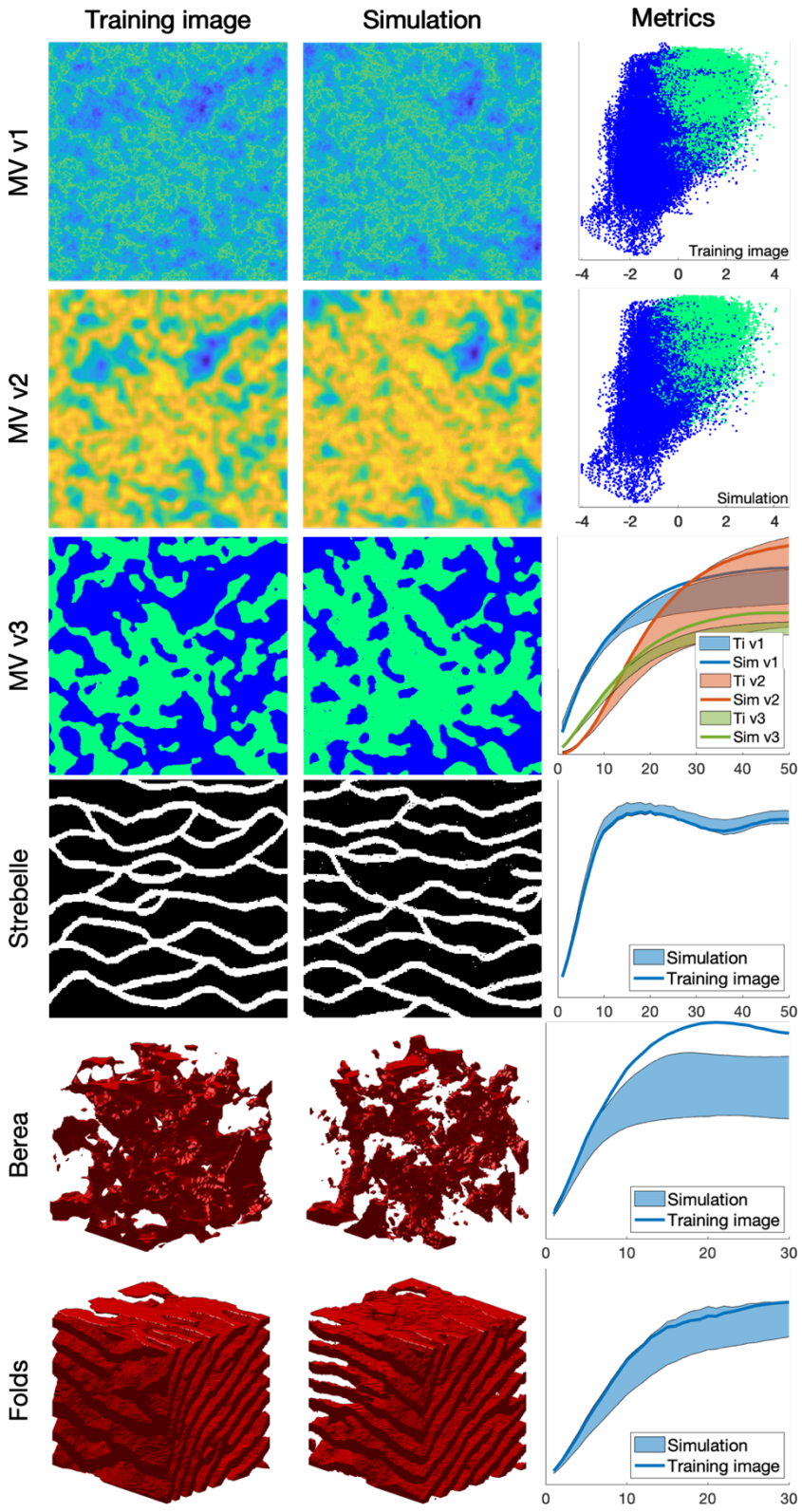


*Figure 3 Examples of unconditional continuous and categorical simulations in 2D and 3D and their variograms. The first column shows the training images that were used, the second column one realization, and the third column quantitative quality metrics. MVs v1, v2 and v3 represent a multivariate training image (and the corresponding simulation) using 3 variables. The first two metrics are scatter plots of MV v1 vs. MV v2 of the training image and the simulation, respectively. The third metric represents the reproduction of the variogram for each of MVs v1, v2 and v3.*

| | MVs v1, v2, v3 | Strebelle | Berea | Folds |
|---|---|---|---|---|
| Source | (Mariethoz and Caers, 2014) | (Strebelle, 2002) | Doi:10.6084/m9.figshare.1153794 | (Mariethoz and Caers, 2014) |
| Size of the training image (px) | $490 \times 490$ | $250 \times 250$ | $100 \times 100 \times 100$ | $180 \times 150 \times 120$ |
| Size of the simulation (px) | $490 \times 490$ | $250 \times 250$ | $100 \times 100 \times 100$ | $180 \times 150 \times 120$ |
| Computation time (s) | 1456 | 54 | 1665 | 76270 |
| $k$ | 1.2 | | | |
| $N$ | 80 | | 125 | |

*Table 1 Parameters that were used for the simulations in Figure 3. Times are specified for simulations without parallelization.*

## 3.2. Comparison with direct sampling simulations

QS simulations are benchmarked against DS using the "Stone" training image (Figure 4). The settings that are used for DS are based on optimal parameters that were obtained via the approach of Baninajar et al. (2019), which uses stochastic optimization to find optimal parameters. In DS, we use a fraction of scanned TI of $f = 1$ to explore the entire training image via the same approach as in QS and we use the $L^2$-norm as in QS. To avoid the occurrence of verbatim copy, we include 0.1% conditioning data, which are randomly sampled from a rotated version of the training image. The number of neighbors $N$ is set to 20 for both DS and QS and the acceptance threshold of DS is set to 0.001.

The comparison is based on qualitative (Figure 5) and quantitative (Figure 6) metrics, which include directional and omnidirectional variograms, along with the connectivity function, the Euler characteristic (Renard and Allard, 2013) and cumulants (Dimitrakopoulos, 2010). The connectivity represents the probability for 2 random pixels to be in the same connected component. This metric is suited to detect broken structures. The Euler characteristic represents the number of objects subtracted by the number of holes of the objects, and is particularly adapted to detect noise in the simulations such as salt and pepper. Cumulants are high order statistics and therefore allow considering the relative positions between elements. The results demonstrate that the simulations are of a quality that is comparable to DS. With extreme settings (highest pattern reproduction regardless of the computation time), both algorithms perform similarly, which is reasonable since both are based on sequential simulation and both directly import data from the training image. The extra noise present in the simulation is shown in the Euler characteristic. Furthermore, it demonstrates that the use of a kernel can reduce this noise to get better simulations.

With QS, kernel weighting allows fine tuning of the parametrization to improve the results, as shown in Figure 5. In this paper, we use an exponential kernel:

*Equation 16*

$$\omega_{\boldsymbol{l}} = e^{-\alpha \|\boldsymbol{l}\|_2}$$

where $\alpha$ is a kernel parameter and $\|.\|_2$ the Euclidean distance. The validation metrics of Figure 6 show that both QS and DS tend to slightly underestimate the variance and the connectivity. Figure 6 shows that an optimal kernel improves the results for all metrics, with all training image metrics in the 5-95% realization interval, except for the Euler characteristic.

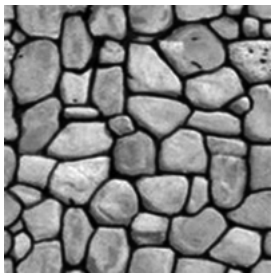

*Figure 4 Training image that was used for benchmarking and sensitivity analysis.*

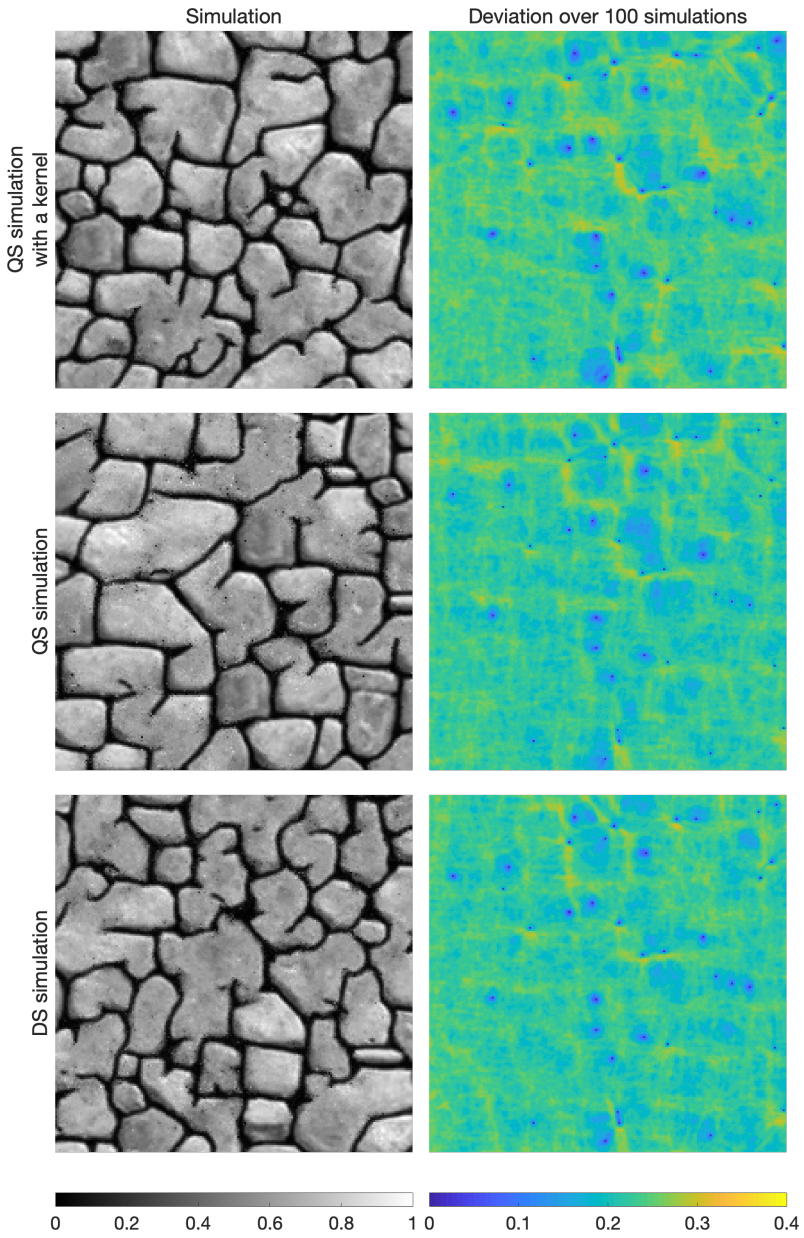


429

430 *Figure 5 Examples of conditional simulations and their standard deviation over 100*
431 *realizations that are used in the benchmark between QS and DS.*

432

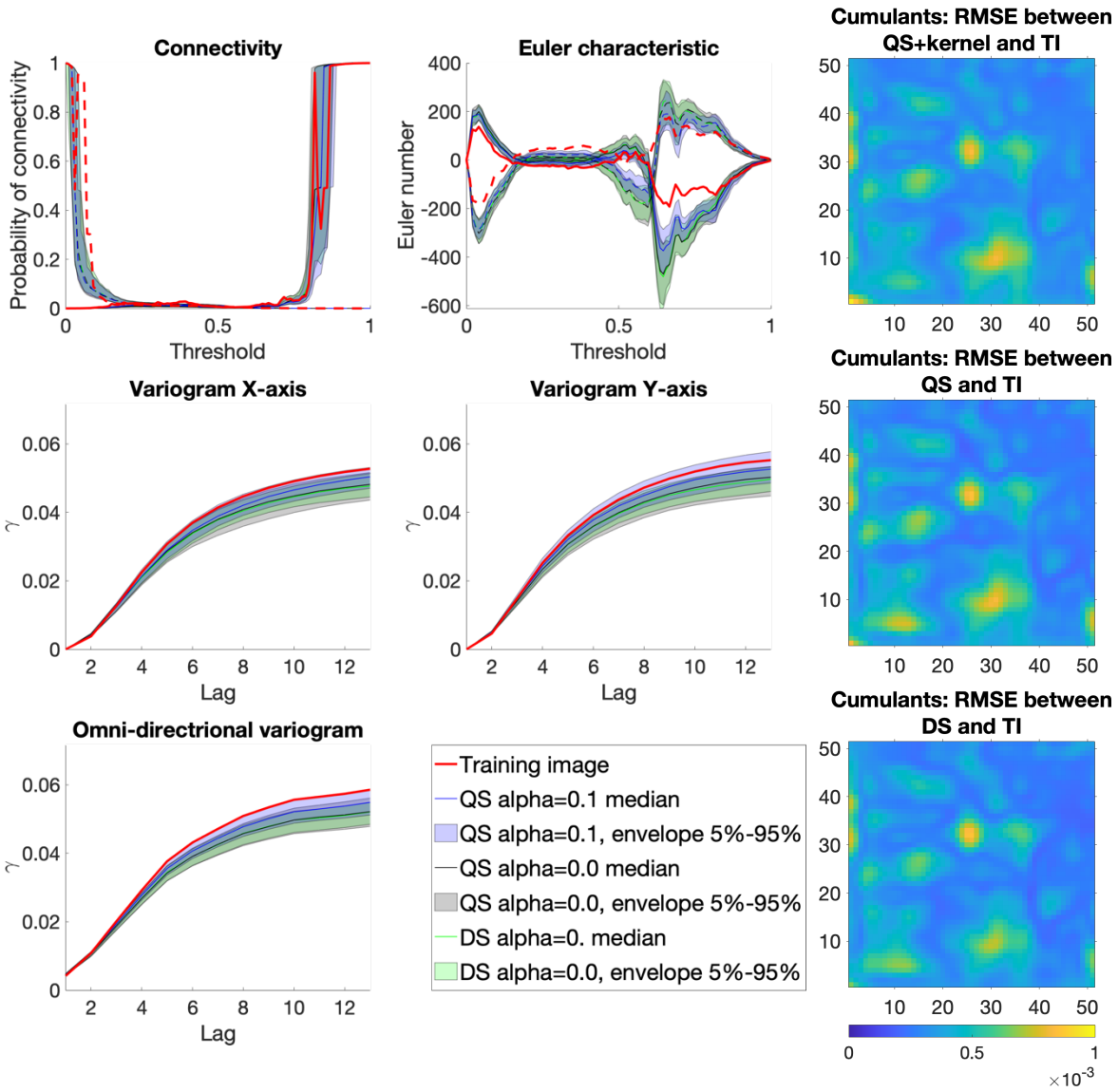


*Figure 6 Benchmark between QS (with and without kernel) and DS over 6 metrics Using each time 100 unconditional simulation.*

## 3.3. Parameter sensitivity analysis

In this section, we perform a sensitivity analysis on the parameters of QS using the training image in Figure 4. Only essential results are reported in this section (Figure 7 and Figure 8); more exhaustive test results are available in Appendix 0 (Figure A 4 and Figure A 5). The two main parameters of QS are the number of neighbors $N$ and the number of used candidates $k$.

Figure 7 (and Appendix 0 Figure A 4) shows that large $N$ values and small $k$ values improve the simulation performance; however, tend to induce verbatim copy in the simulation. Small values of $N$ result in noise with good reproduction of the histogram.

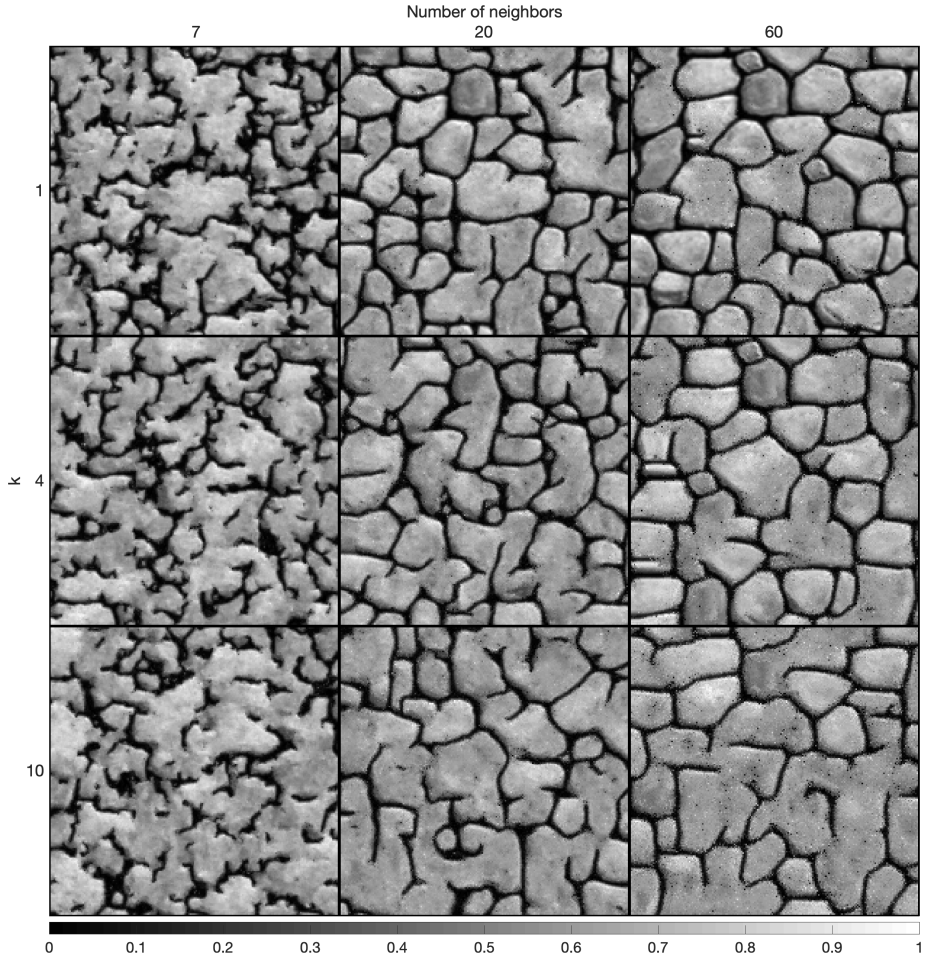


*Figure 7 Sensitivity analysis on one simulation for the two main parameters of QS using a uniform kernel.*

$\omega$ can be a very powerful tool, typically using the assumption that the closest pixels are more informative than remote pixels. The sensitivity analysis of the kernel value $\alpha$ are explored in Figure 8 and Figure A 5. They show that α provides a unique tool for improving the simulation quality. In particular, using a kernel can reduce the noise in simulations, which is clearly visible by comparing the Euler characteristic curves. However, reducing too much the importance of distant pixels results in ignoring them altogether, therefore damaging long-range structures.

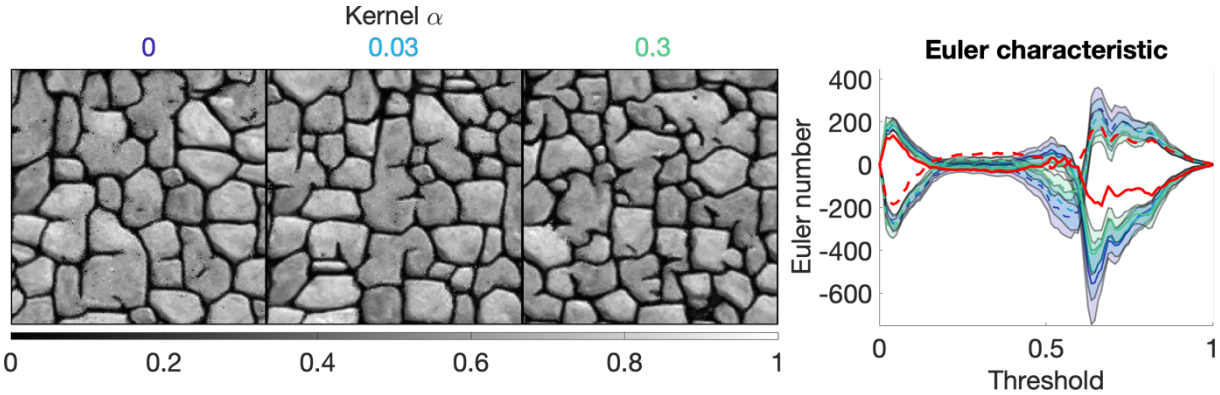


*Figure 8 Sensitivity analysis on the kernel parameter α, with fixed parameters k=1.5 and N=40. The values of the kernels are shown in colors that correspond to the Euler characteristic lines (red is the training image).*

## 3.4. Computational efficiency and scalability

In this section, we investigate the scalability of QS with respect to the size of the simulation grid, the size of the training image grid, the number of variables, incomplete training images, and hardware. According to the test results, the code will continue to scale with new-generation hardware.

As explained in Section 2.3 and 2.4, the amounts of time that are consumed by the two main operations of QS (finding candidates and sorting them) are independent of the pixel values. Therefore, the training image that is used is not relevant (here, we use simulations that were performed with the TI of Figure 4 and its classified version for categorical cases). Furthermore, the computation time is independent of the parametrization ($k$ and $N$). However, the performance is affected by the type of mismatch function that is used; here, we consider both continuous (Equation 2 and Equation 14) and categorical cases (Equation 3 and Equation 15).

We also test our implementation on different types of hardware, as summarized in Table 2. We expect Machine (2) to be faster than Machine (1) for medium-sized problems due to the high memory bandwidth requirement of QS. Machine (3) should also be faster than Machine (1) because it takes advantage of a longer vector computation (512-bit VS. 256-bit instruction set).

| Name of the machine | Machine (1) | Machine (2) | Machine (3) |
|---|---|---|---|
| CPU | -2x Intel(R) Xeon(R) CPU E5-2680 v2 @ 2.80 GHz | -Xeon Phi, Intel(R) Xeon Phi (TM) CPU 7210 @ 1.30 GHz | -2x Intel(R) Xeon(R) Gold 6128 Processor @ 3.40 GHz |
| Memory type | - DDR3 | - MCDRAM / DDR4 | - DDR4 |
| OS, compiler and compilation flags | Linux, Intel C/C++ compiler 2018 with -xhost | | |

*Table 2 Hardware that was used in the experiments*

Figure 9 plots the execution times on the 3 tested machines for continuous and categorical cases and with training images of various sizes. Since QS has a predictable execution time, the influence of the parameters on the computation time is predictable: linear with respect to the number of variables (Figure 9a, Figure 9b), linear with respect to the size of the simulation grid and following a power function of the size of the training image (Figure 9c). Therefore, via a few tests on a set of simulations, one can predict the computation time for any other setting.

Figure 9d shows the scalability of the algorithm when using the path-level parallelization. The algorithm scales well until all physical cores are being used. Machine (3) has a different scaling factor (slope). This suboptimal scaling is attributed to the limited memory bandwidth. Our implementation of QS scales well with an increasing number of threads (Figure 9d), with an efficiency above 80% using all possible threads. The path-level parallelization strategy that was used involves a bottleneck for large number of threads due to the need to wait for neighborhood conflicts to be resolved (Mariethoz 2010). This effect typically appears for large values of $N$ or

intense parallelization (>50 threads) on small grids. It is assumed that small grids do not require intense parallelization; hence, this problem is irrelevant in most applications.

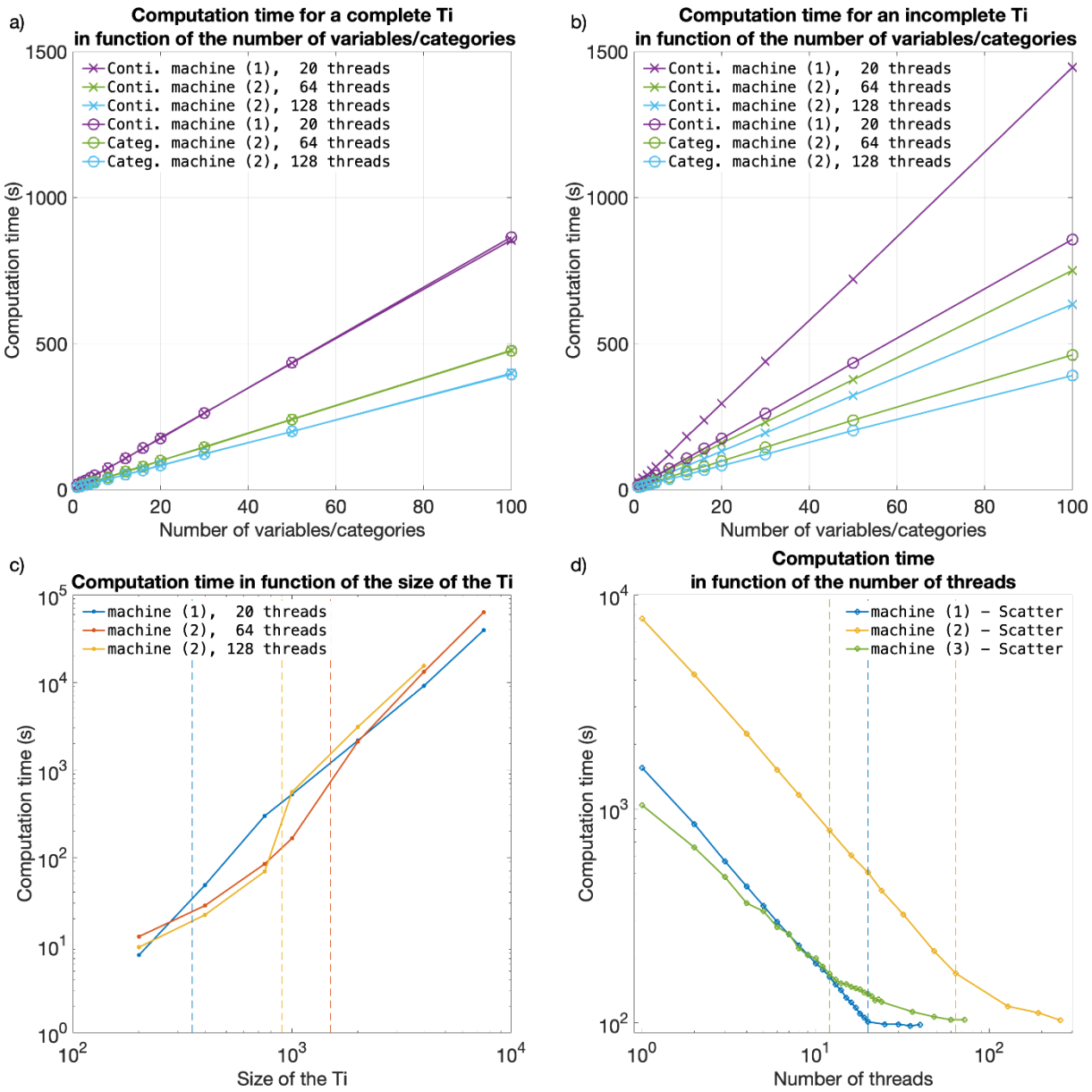


*Figure 9 Efficiency of QS with respect to all key parameters. a) and b) are the evolution of the computation time for complete and incomplete training images, respectively, with continuous and categorical variables. c) shows the evolution of the computation time as the size of the training image is varied; the dashed lines indicate that the training image no longer fits in the CPU cache. d) shows the evolution of the computation time as the number of threads is increased. The dashed lines indicate that all physical cores are used.*

## 4. Discussion

The parameterization of the algorithm (and therefore simulation quality) has almost no impact on the computational cost, which is an advantage. Indeed, many MPS algorithms impose trade-

offs between the computation time and the parameters that control the simulation quality, thereby imposing difficult choices for users. QS is comparatively simpler to set up in this regard. In practice, a satisfactory parameterization strategy is often to start with a small $k$ value (say 1.2) and a large $N$ value ($> 50$) and then gradually change these values to increase the variability if necessary (Figure 6 and Figure A 4).

QS is adapted for simulating continuous variables using the $L^2$-norm. However, a limitation is that the $L^1$-norm does not have a decomposition that satisfies Equation 1 and, therefore, cannot be used with QS. Another limitation is that for categorical variables, each class requires a separate FFT, which incurs an additional computational cost. This renders QS less computationally efficient for categorical variables (if there are more than 2 categories) than for continuous variables. For accelerated simulation of categorical variables, a possible alternative to reduce the number of required operations is presented in Appendix A.2. The strategy is to use encoded variables, which are decoded in the mismatch map. While this alternative yields significant computational gains, it does not allow the use of a kernel weighting and is prone to numerical precision issues.

Combining multiple continuous and categorical variables can be challenging for MPS approaches. Several strategies have been developed to overcome this limitation, using either a different distance threshold for each variable, or a linear combination of the errors. Here we use the second approach, taking advantage of the linearity of the Fourier transform. The relative importance can be set in $f_i$ and $g_i$ functions in Equation 1. However, it is computationally advantageous to use the kernel weights in order to have standard functions for each metric. Setting such variable-dependent parameters is complex. Therefore in order to find optimal parameters, stochastic optimization approaches (such as Baninajar et al., 2019) are applied to QS. The computational efficiency of QS is generally advantageous compared to other pixel-based algorithms: for example, in our tests it performed faster than DS. QS requires more memory than DS, especially for applications with categorical variables with many classes and with a path-level parallelization. However, the memory requirement is much lower compared to MPS algorithms that are based on a pattern database, such as SNESIM.

There may be cases where QS slower than DS, in particular when using a large training image that is highly repetitive. In such cases, using DS can be advantageous as it must scan only a very small part of the training image. For scenarios of this type, it is possible to adapt QS such that only a small subset of the training image is used; this approach is described in Appendix A3. In the cases of highly repetitive training images, this observation remains true also for SNESIM and IMPALA.

Furthermore, QS is designed to efficiently handle large and complex training images (up to 10 million pixels), with high variability of patterns and few repetitions. Larger training images may be computationally burdensome, which could be alleviated by using a GPUs implementation allowing gains up to two orders of magnitude.

QS can be extended to handle the rotation and scaling of patterns by applying a constant rotation or affinity transformation to the searched patterns (Strebelle, 2002). However, the use rotation-invariant distances and affinity-invariant distances (as in Mariethoz and Kelly, 2011), while possible in theory, would substantially increase the computation time. Mean-invariant distances

can be implemented by simply adapting the distance formulation in QS. All these advanced features are outside the scope of this paper.

## 5. Conclusions

QS is an alternative approach for performing $n$-dimensional pixel-based simulations, which uses an $L^2$-distance for continuous cases and an $L^0$-distance for categorical data. The framework is highly flexible and allows other metrics to be used. The simple parameterization of QS renders it easy to use for nonexpert users. Compared to other pixel-based approaches, QS has the advantage of generating realizations in constant and predictable time for a specified training image size. Using the quantile as a quality criterion naturally reduces the small-scale noise compared to DS. In terms of parallelization, the QS code scales well and can adapt to new architectures due to the use of external highly optimized libraries.

The QS framework provides a complete and explicit mismatch map, which can be used to formulate problem-specific rules for sampling or even solutions that take the complete conditional probability density function into account, for example, such as a narrowness criterion for the conditional pdf of the simulated value (Gravey et al., 2019; Rasera et al., 2019), or to use the mismatch map to infer the optimal parameters of the algorithm.

## 6. Code availability

The source code and documentation of the QS simulation algorithm are available as part of the G2S package at: https://github.com/GAIA-UNIL/G2S under GPLv3 license. Or permanently at https://doi.org/10.5281/zenodo.3546338

Platform: Linux / macOS / Windows 10 Language: C/C++

Interfacing functions in MATLAB, Python3, R

A package is available with our unbiased partial sort at: https://github.com/mgravey/randomKmin-max

## 7. Author contribution

MG proposed the idea, implemented and optimized the QS approach and wrote the manuscript. GM provided supervision, methodological insights and contributed to the writing of the manuscript.

# 8. Appendices

## A.1. Partial sorting with random sampling

Standard partial sorting algorithms resolve tie ranks deterministically, which does not accord with the objective of stochastic simulation with QS, where variability is sought. Here, we propose an online heap-based partial sort. It is realized with a single scan of the array of data using a heap to store previously found values. This approach is especially suitable when we are interested in a small fraction of the entire array.

Random positions of the $k$ best values are ensured by swapping similar values. If $k = 1$, the saved value is switched with a smaller value each time it is encountered. If an equal value is scanned, a counter $c$ is increased for this specific value and a probability of $1/c$ of switching to the new position is applied. If $k > 1$, the same strategy is extended by carrying over the counter $c$.

This partial sort outperforms random exploration of the mismatch map. However, it is difficult to implement efficiently on GPUs. A solution is still possible for shared-memory GPUs by performing the partial sort on the CPU. This is currently available in the proposed implementation.

$k$: the number of values of interest
$D$: the input data array
$S$: the array with the $k$ smallest values (sorted)
$Sp$: the array with the positions that are associated with the values of $S$

1. **for** each value $v$ of $D$
2. **if** $v$ is smaller than the smallest value of $S$
3. search in $S$ for the position $p$ at which to insert $v$ and insert it
4. **if** $p = k$ // last position of the array
5. reinitialize the counter $c$ to 0
6. insert $v$ at the last position
7. **else**
8. increment $c$ by one
9. swap the last position with another of the same value
10. insert the value at the expected position $p$
11. **end**
12. **else** if $v$ is equal to the smallest value of $S$
13. increment $c$ by one
14. change the position of $v$ to one of the $n$ positions of equal value with a probability of $n/(n + c)$
15. **end**
16. **end**

## A.2. Encoded categorical variables

To handle categorical variables, a standard approach is to consider each category as an independent variable. This requires as many FFTs as classes. This solution renders it expensive to use QS in cases with multiple categories.

An alternative approach is to encode the categories and to decode the mismatch from the cross-correlation. It has the advantage of only requiring only a single cross-correlation for each simulated pattern.

Here, we propose encoding the categories as powers of the number of neighbors, such that their product is equal to one if the class matches. In all other cases, the value is smaller than one or larger than the number of neighbors.

$$\varepsilon_{L^0}(a,b) = \psi\left((a-b)^0 \propto -(N+1)^{-p(a)}.(N+1)^{-p(b)}\right)$$

where $N$ is the largest number of neighbors that can be considered and $p(c)$ is an arbitrary function that maps index classes of $\mathcal{C}$, $c \in \mathcal{C}$.

In this scenario, in Equation 1 this encoded distance $L_e^0$ can be decomposed into the following series of functions $f_j$ and $g_j$ :

$$f_0 : x \to -(N+1)^{p(x)}$$

$$g_0 : x \to (N+1)^{-p(x)}$$

and the decoding function is

$$\psi(x) = \lfloor x \rceil \bmod N$$

Table A 1 describes this process for 3 classes, namely, $a, b,$ and $c$, and a maximum of 9 neighbors. Then, the error can be easily decoded by removing decimals and dozens.

| Products | $g_0(a) = 1$ | $g_0(b) = 0.1$ | $g_0(c) = 0.01$ |
|---|---|---|---|
| $f_0(a) = 1$ | **1** | 0.1 | 0.01 |
| $f_0(b) = 10$ | 10 | **1** | 0.1 |
| $f_0(c) = 100$ | 100 | 10 | **1** |

*Table A 1 Example of encoding for 3 classes and 9 neighbors and their associated products*

Consider the following combination:

$$f_0(a,\ b,\ a,\ c,\ c,\ b,\ a,\ a,\ b)$$
$$\times\ g_0(c,\ b,\ b,\ a,\ a,\ b,\ c,\ a,\ a)$$
$$-(0.01,\ 1,\ 0.1, 100, 100,\ 1, 0.01,\ 1,\ 10) = -213.12$$

The decoding $\lfloor -213.12 \rceil \bmod 10 = -213 \bmod 10 = -3$ yields 3 matches (in green).

This encoding strategy provides the possibility of drastically reducing the number of FFT computations. However, the decoding phase is not always implementable if a nonuniform matrix $\omega$ is used. Finally, the test results show that the method suffers quickly from numerical precision issues, especially with many classes.

## A.3. Sampling strategy using training image splitting

The principle of considering a fixed number of candidates can be extended by instead of taking the $k^{th}$ best candidate, sampling the best candidate in only a portion $\frac{1}{k}$, of the TI. For instance, as an alternative to considering $k = 4$, this strategy searches for the best candidate in one fourth of the image. This is more computationally efficient. However, if all the considered candidates are contiguous (by splitting the TI in $k$ chunks), this approximation is only valid if the TI is completely stationary and all $k$ equal subdivisions of the TI are statistically identical. In practice, real-world continuous variables are often nonstationary. However, in categorical cases, especially in binary ones, the number of pattern replicates is higher and this sampling strategy could be interesting.

The results of applying this strategy are presented in Table A 2 and Figure A 1. The experimental results demonstrate that the partial exploration approach that is provided by splitting substantially accelerates the processing time. However, Figure A 1 shows that the approach has clear limitations when dealing with training images with complex and

nonrepetitive patterns. The absence of local verbatim copy can explain the poor-quality simulation results.

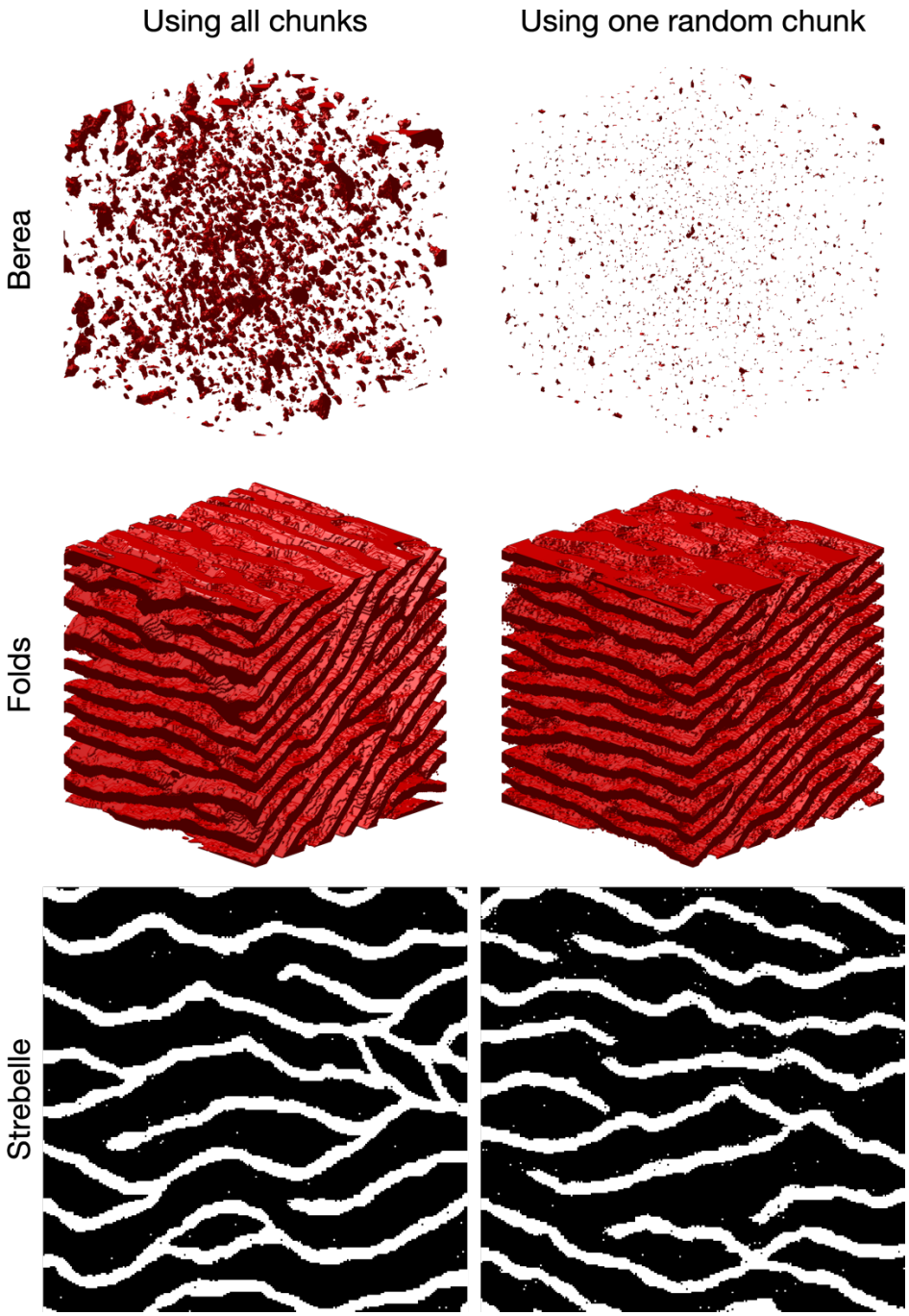


*Figure A 1 Comparison of QS using the entire training image and using training image splitting. In these examples, the training image is split into two images over each dimension. The original training images are presented in Figure 2.*

| Training image | Using all chunks | Using one random chunk | Speedup |
|---|---|---|---|
| Berea | 11 052 s | 1 452 s | 7.61x |
| Folds | 35 211 s | 4 063 s | 8.66x |
| Strebelle | 7.95 s | 3.16 s | 2.51x |

*Table A 2 Computation times and speedups for the full and partial exploration approaches. Times are specified for simulations with path level parallelization.*

## A.4. Additional results

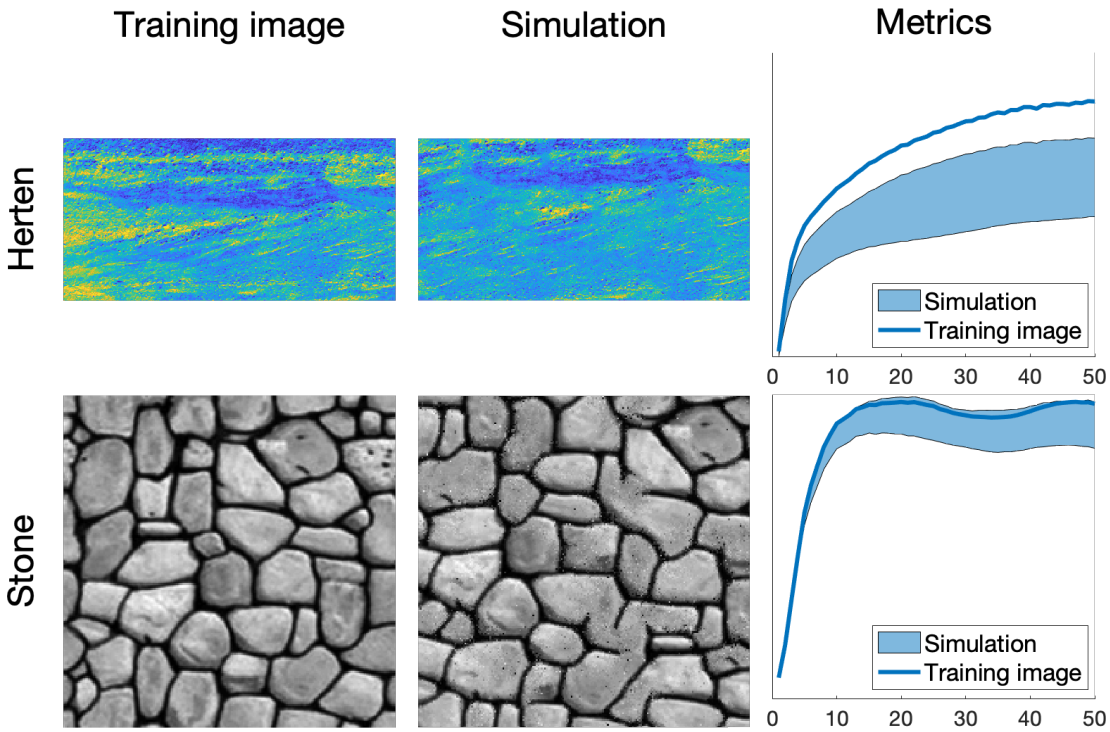


*Figure A 2 Examples of 2D simulations: the first 3 rows represent 3 variables of a single simulation. Parameters available in Table A 3*

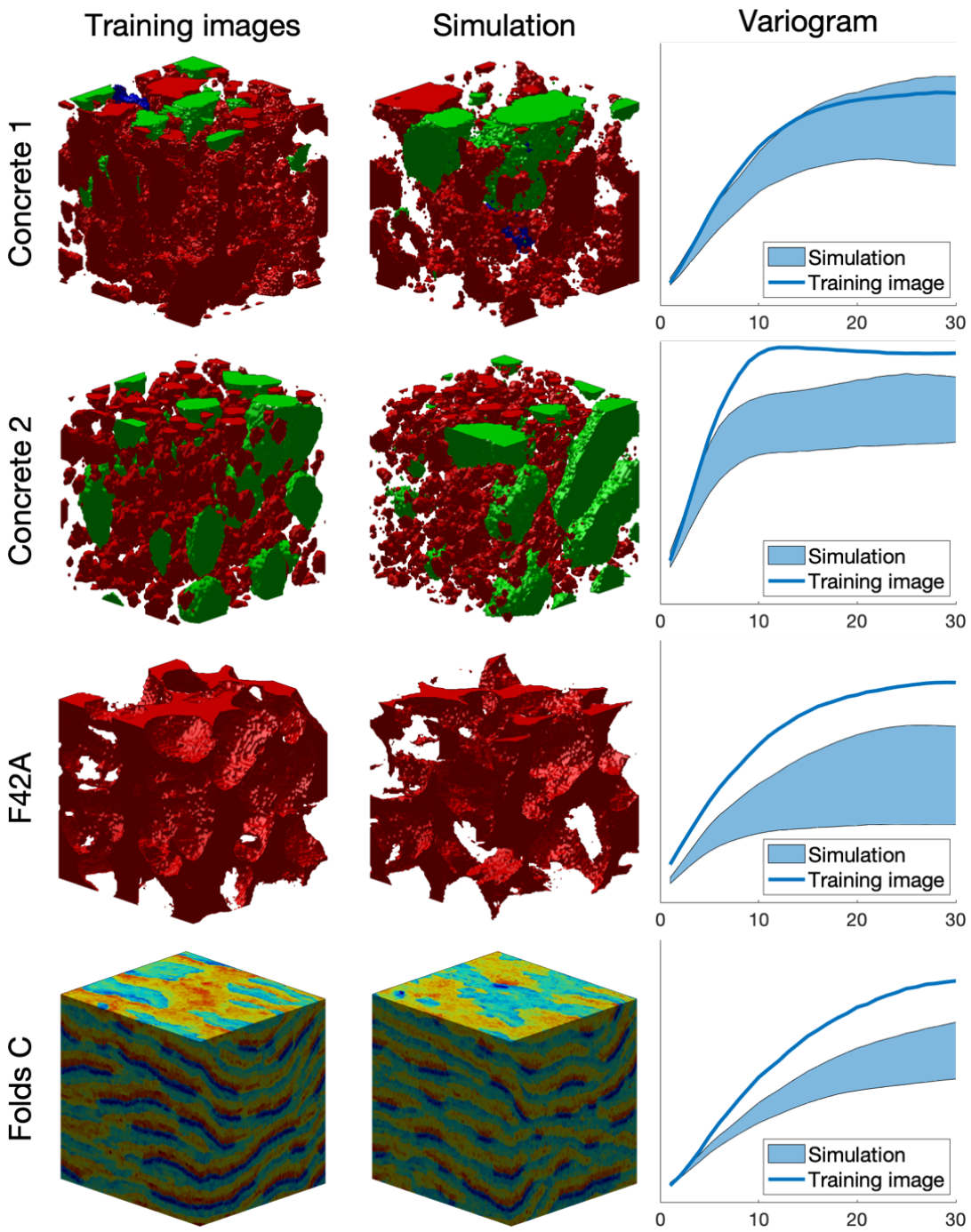


*Figure A 3 Examples of 3D simulation results. Parameters available in Table A 4*

| | Herten | Stone |
|---|---|---|
| Source | (Mariethoz and Caers, 2014) | (Mariethoz and Caers, 2014) |
| Size of the training image (px) | $716 \times 350$ | $200 \times 200$ |
| Size of the Simulation (px) | $716 \times 350$ | $200 \times 200$ |
| Computation time (s) | 1133 | 21 |
| $k$ | 1.2 | |
| $N$ | 80 | |

*Table A 3 Simulation parameters for Figure A 2. Times are specified for simulations without parallelization.*

| | Concrete 1 | Concrete 2 | F42A | Folds continues |
|---|---|---|---|---|
| Source | (Meerschman et al., 2013) | (Meerschman et al., 2013) | Doi:10.6084/m9.figshare.1189259 | (Mariethoz and Caers, 2014) |
| Size of the training image (px) | $150 \times 150 \times 150$ | $100 \times 90 \times 80$ | $100 \times 100 \times 100$ | $180 \times 150 \times 120$ |
| Size of the simulation (px) | $100 \times 100 \times 100$ | $100 \times 100 \times 100$ | $100 \times 100 \times 100$ | $180 \times 150 \times 120$ |
| Computation time (s) | 11436 | 1416 | 1638 | 7637 |
| $k$ | 1.2 | | | |
| $N$ | 50 | | 125 | |

*Table A 4 Simulation parameters for Figure A 3. Times are specified for simulations without parallelization.*

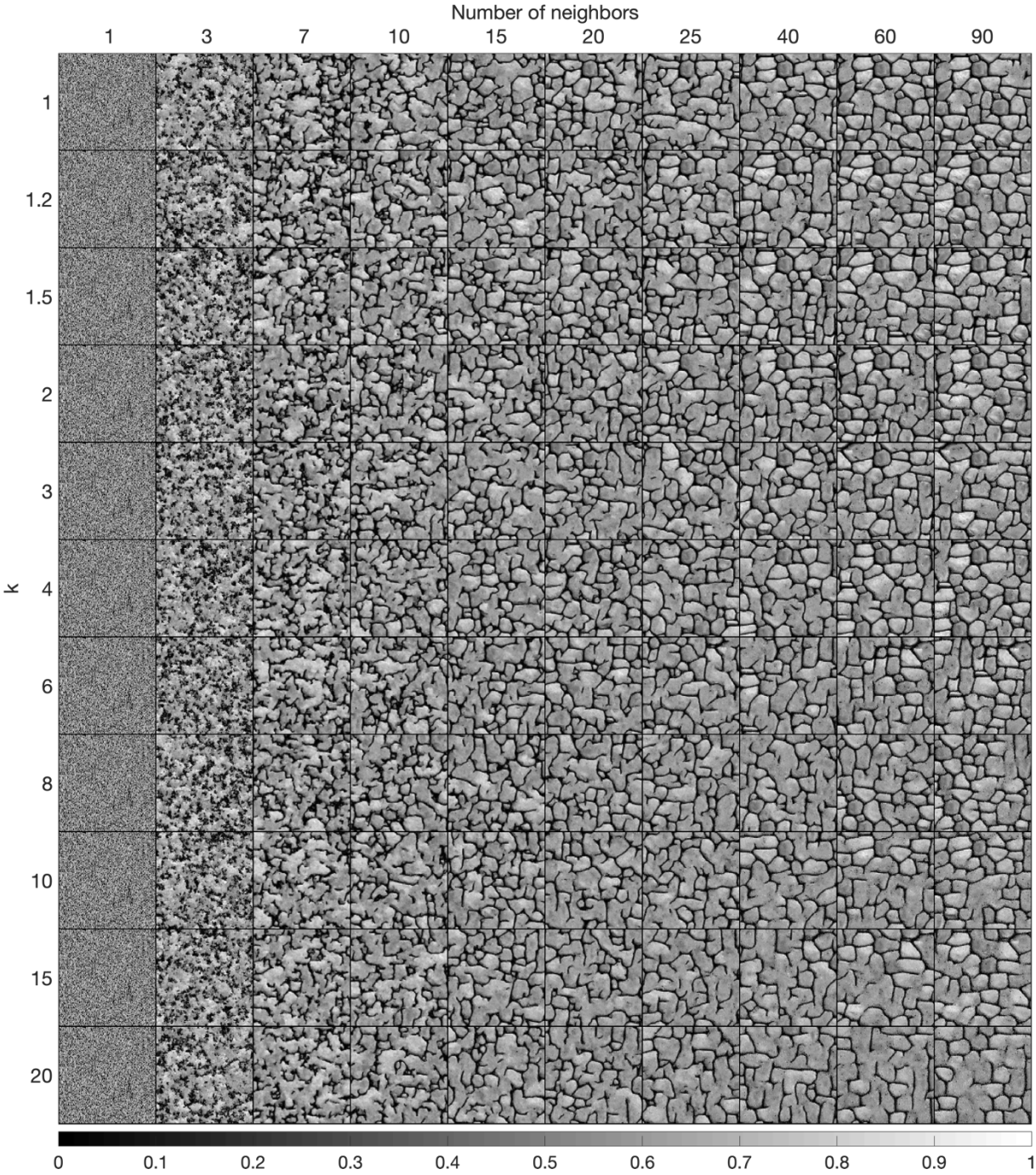


677

678 *Figure A 4 Complete sensitivity analysis, with one simulation for the two main parameters of*
679 *QS.*

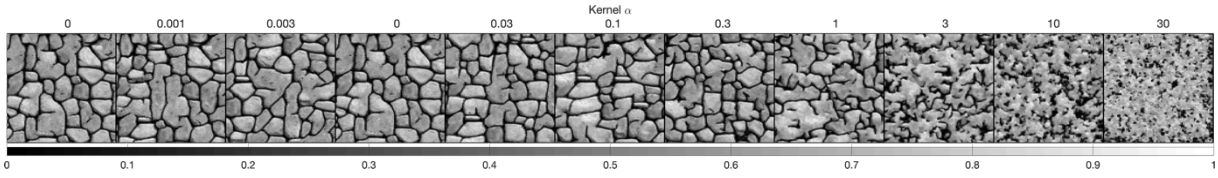


680

681 *Figure A 5 Complete sensitivity analysis, with one simulation for each kernel with k=1.5 and*
682 *N=40*

## A.5. Mathematical derivation

The convolution theorem (Stockham, 1966; Krant, 1999; Li et al., 2019) can be easily extended to cross-correlation(Bracewell, 2000). The flowing derivation shows the validity of the theorem for any function f and g.

$$\mathcal{F}\{f \star g\} = \int (f \star g)(t) e^{it.\xi} dt = \int \int \overline{f(s)} g(s+t) ds\, e^{it.\xi} dt$$

$$= \int \int \overline{f(s)} e^{i(-s).\xi} ds.\, g(s+t) ds\, e^{i(t+s).\xi} dt$$

$$= \int \int \overline{f(s) e^{i(s).\xi}} ds.\, g(s+t) ds\, e^{i(t+s).\xi} dt = \overline{\mathcal{F}\{f\}}.\mathcal{F}\{f\}$$

The discretization of this property can be obtained using two piecewise continuous functions associated to each discrete representation.

## 9. Acknowledgments

This research was funded by the Swiss National Science Foundation, grant number 200021_162882. Thanks to Intel for allowing us to conduct numerical experiments on their latest hardware using the AI DevCloud. Thanks to Luiz Gustavo Rasera for his comments, which greatly improved the manuscript; to Dr. Ehsanollah Baninajar for running his optimization method, which improved the reliability of the benchmarks; and to all the early users of QS for their useful feedback and their patience in waiting for this manuscript. A particular thanks to Prof. Ute Mueller and Prof. Thomas Mejer Hansen that accepted to review the paper and provided constructive comments which significantly improved the quality of the paper.

## 10.References

Arpat, G. B. and Caers, J.: Conditional Simulation with Patterns, Mathematical Geology, 39(2), 177–203, doi:10.1007/s11004-006-9075-3, 2007.

Bancheri, M., Serafin, F., Bottazzi, M., Abera, W., Formetta, G. and Rigon, R.: The design, deployment, and testing of kriging models in GEOframe with SIK-0.9.8, Geosci. Model Dev., 11(6), 2189–2207, doi:10.5194/gmd-11-2189-2018, 2018.

Baninajar, E., Sharghi, Y. & Mariethoz, G.: MPS-APO: a rapid and automatic parameter optimizer for multiple-point geostatistics, Stoch Environ Res Risk Assess, 33: 1969–1989, doi:10.1007/s00477-019-01742-7, 2019

Barfod, A. A. S., Vilhelmsen, T. N., Jørgensen, F., Christiansen, A. V., Høyer, A.-S., Straubhaar, J. and Møller, I.: Contributions to uncertainty related to hydrostratigraphic modeling using multiple-point statistics, Hydrol. Earth Syst. Sci., 22(10), 5485–5508, doi:10.5194/hess-22-5485-2018, 2018.

Blagodurov, S., Fedorova, A., Zhuravlev, S., & Kamali, A.: A case for NUMA-aware contention management on multicore systems. In 2010 19th International Conference on Parallel Architectures and Compilation Techniques (PACT) (pp. 557-558), IEEE, 2010.

Bracewell, R. N.: The fourier transform and its applications. Boston: McGraw-hill, 2000

Cooley, J. W., computation, J. T. M. O.1965: An algorithm for the machine calculation of complex Fourier series, JSTOR, 19(90), 297, doi:10.2307/2003354, 1965.

Dimitrakopoulos, R., Mustapha, H. & Gloaguen, E.: High-order Statistics of Spatial Random Fields: Exploring Spatial Cumulants for Modeling Complex Non-Gaussian and Non-linear Phenomena. Math Geosci 42, 65, doi: 10.1007/s11004-009-9258-9, 2010

Dong, H. and Blunt, M. J.: Pore-network extraction from micro-computerized-tomography images, Phys. Rev. E, 80(3), 84–11, doi:10.1103/PhysRevE.80.036307, 2009.

Frigo, M. and Johnson, S. G.: FFTW, [online] Available from: http://www.fftw.org/fftw3.pdf, 2018.

Gauss, C. F.: Demonstratio nova theorematis omnem functionem algebraicam. 1799.

Gómez-Hernández, J. J. and Journel, A. G.: Joint Sequential Simulation of MultiGaussian Fields, in Geostatistics Tróia '92, vol. 5, pp. 85–94, Springer, Dordrecht, Dordrecht. 1993.

Graeler, B., Pebesma, E. and Heuvelink, G.: Spatio-Temporal Interpolation using gstat, R Journal, 8(1), 204–218, 2016.

Gravey, M., Rasera, L. G. and Mariethoz, G.: Analogue-based colorization of remote sensing images using textural information, ISPRS Journal of Photogrammetry and Remote Sensing, 147, 242–254, doi:10.1016/j.isprsjprs.2018.11.003, 2019.

Guardiano, F. B. and Srivastava, R. M.: Multivariate Geostatistics: Beyond Bivariate Moments, in Geostatistics Tróia '92, vol. 5, pp. 133–144, Springer, Dordrecht, Dordrecht. 1993.

Hamming, R. W.: Error detecting and error correcting codes, edited by The Bell system technical, The Bell system technical, 29(2), 147–160, doi:10.1002/j.1538-7305.1950.tb00463.x, 1950.

Hoffimann, J., Scheidt, C., Barfod, A., Caers, J.2017: Stochastic simulation by image quilting of process-based geological models, Elsevier, doi:10.1016/j.cageo.2017.05.012, 2017.

Honarkhah, M. and Caers, J.: Stochastic Simulation of Patterns Using Distance-Based Pattern Modeling, Math Geosci, 42(5), 487–517, doi:10.1007/s11004-010-9276-7, 2010.

Intel Corporation: Intel® Math Kernel Library Reference Manual - C, 1–2606, 2019.

Jha, S. K., Mariethoz, G., Evans, J., McCabe, M. F. and Sharma, A.: A space and time scale-dependent nonlinear geostatistical approach for downscaling daily precipitation and temperature, Water Resources Research, 51(8), 6244–6261, doi:10.1002/2014WR016729, 2015.

John Paul Shen, M. H. L.: Modern Processor Design: Fundamentals of Superscalar Processors, 1–658, 2018.

Krantz, S. G.: A panorama of harmonic analysis. Washington, D.C.: Mathematical Association of America, 1999

Latombe, G., Burke, A., Vrac, M., Levavasseur, G., Dumas, C., Kageyama, M. and Ramstein, G.: Comparison of spatial downscaling methods of general circulation model results to study climate variability during the Last Glacial Maximum, Geosci. Model Dev., 11(7), 2563–2579, doi:10.5194/gmd-11-2563-2018, 2018.

Li, B., & Babu, G. J.: A graduate course on statistical inference. New York: Springer, 2019

Li, J. and Heap, A. D.: Spatial interpolation methods applied in the environmental sciences: A review, Environ Model Softw, 53(C), 173–189, doi:10.1016/j.envsoft.2013.12.008, 2014.

Li, X., Mariethoz, G., Lu, D. and Linde, N.: Patch-based iterative conditional geostatistical simulation using graph cuts, Water Resources Research, 52(8), 6297–6320, doi:10.1002/2015WR018378, 2016.

Mahmud, K., Mariethoz, G., Caers, J., Tahmasebi, P. and Baker, A.: Simulation of Earth textures by conditional image quilting, Water Resources Research, 50(4), 3088–3107, doi:10.1002/2013WR015069, 2014.

Mariethoz, G.: A general parallelization strategy for random path based geostatistical simulation methods, Computers and Geosciences, 36(7), 953–958, doi:10.1016/j.cageo.2009.11.001, 2010.

Mariethoz, G. and Caers, J.: Multiple-point geostatistics: stochastic modeling with training images, Wiley. 2014.

Mariethoz, G. and Kelly, B. F. J.: Modeling complex geological structures with elementary training images and transform-invariant distances, Water Resources Research, 47(7), 959–14, doi:10.1029/2011WR010412, 2011.

Mariethoz, G. and Lefebvre, S.: Bridges between multiple-point geostatistics and texture synthesis_ Review and guidelines for future research, Computers and Geosciences, 66(C), 66–80, doi:10.1016/j.cageo.2014.01.001, 2014.

Mariethoz, G., Renard, P. and Straubhaar, J.: The Direct Sampling method to perform multiple-point geostatistical simulations, Water Resources Research, 46(11), doi:10.1029/2008WR007621, 2010.

Matheron, G.: The intrinsic random functions and their applications, Advances in Applied Probability, 5(3), 439–468, doi:10.2307/1425829, 1973.

Meerschman, E., Pirot, G., Mariethoz, G., Straubhaar, J., Van Meirvenne, M. and Renard, P.: A practical guide to performing multiple-point statistical simulations with the Direct Sampling algorithm, Computers and Geosciences, 52(C), 307–324, doi:10.1016/j.cageo.2012.09.019, 2013.

Oriani, F., Ohana-Levi, N., Marra, F., Straubhaar, J., Mariethoz, G., Renard, P., Karnieli, A. and Morin, E.: Simulating Small-Scale Rainfall Fields Conditioned by Weather State and Elevation: A Data-Driven Approach Based on Rainfall Radar Images, Water Resources Research, 15(4), 265, doi:10.1002/2017WR020876, 2017.

Rasera L.G., Gravey M., Lane S. N., Mariethoz G. Downscaling images with trends using multiple-point statistics simulation: An application to digital elevation models, Mathematical Geosciences, 1– 43, doi:10.1007/s11004-019-09818-4, 2019

Renard, P. and Allard, D.: Connectivity metrics for subsurface flow and transport, Advances in Water Resources, 51(C), 168–196, doi:10.1016/j.advwatres.2011.12.001, 2013.

Rodríguez, P.: A radix-2 FFT algorithm for modern single instruction multiple data (SIMD) architectures, doi:10.1109/ICASSP.2002.5745335, 2002.

Shannon: A mathematical theory of communication, Wiley Online Library, 1948.

Straubhaar, J., Renard, P., Mariethoz, G., Froidevaux, R. and Besson, O.: An Improved Parallel Multiple-point Algorithm Using a List Approach, Math Geosci, 43(3), 305–328, doi:10.1007/s11004-011-9328-7, 2011.

Strebelle, S.: Conditional simulation of complex geological structures using multiple-point statistics, Mathematical Geology, 34(1), 1–21, doi:10.1023/A:1014009426274, 2002.

Strebelle, S., Payrazyan, K. and Caers, J.: Modeling of a Deepwater Turbidite Reservoir Conditional to Seismic Data Using Multiple-Point Geostatistics, Society of Petroleum Engineers. 2002.

Stockham, T. G., Jr.: High-speed convolution and correlation. Proceedings of the April 26-28, 1966, Spring Joint Computer Conference on XX - AFIPS '66 (Spring). Presented at the the April 26-28, 1966, Spring joint computer conference, doi:10.1145/1464182.1464209, 1966

Tadić, J. M., Qiu, X., Miller, S. and Michalak, A. M.: Spatio-temporal approach to moving window block kriging of satellite data v1.0, Geosci. Model Dev., 10(2), 709–720, doi:10.5194/gmd-10-709-2017, 2017.

Tadić, J. M., Qiu, X., Yadav, V. and Michalak, A. M.: Mapping of satellite Earth observations using moving window block kriging, Geosci. Model Dev., 8(10), 3311–3319, doi:10.5194/gmd-8-3311-2015, 2015.

Tahmasebi, P.: Structural Adjustment for Accurate Conditioning in Large-Scale Subsurface Systems, Advances in Water Resources, 1–52, doi:10.1016/j.advwatres.2017.01.009, 2017.

Tahmasebi, P., Sahimi, M., Mariethoz, G. and Hezarkhani, A.: Accelerating geostatistical simulations using graphics processing units (GPU), Computers and Geosciences, 46(C), 51–59, doi:10.1016/j.cageo.2012.03.028, 2012.

Vannametee, E., Babel, L. V., Hendriks, M. R., Schuur J.: Semi-automated mapping of landforms using multiple point geostatistics, Elsevier, doi:10.1016/j.geomorph.2014.05.032, 2014.

825 Wojcik, R., McLaughlin, D., on, A. K. I. T.2009: Conditioning stochastic rainfall replicates
826 on remote sensing data, doi:10.1109/TGRS.2009.2016413, 2009.

827 Yin, G., Mariethoz, G. and McCabe, M.: Gap-Filling of Landsat 7 Imagery Using the Direct
828 Sampling Method, Remote Sensing, 9(1), 12, doi:10.3390/rs9010012, 2017.